



## Validation and sensitivity of model-predicted proximal tibial displacement and tray micromotion in cementless total knee arthroplasty under physiological loading conditions

Huizhou Yang <sup>a</sup>, Riza Bayoglu <sup>a</sup>, Mohsen Sharifi Renani <sup>a</sup>, Yashar Behnam <sup>a</sup>, Alessandro Navacchia <sup>a</sup>, Chadd Clary <sup>a</sup>, Paul J. Rullkoetter <sup>a,\*</sup>

<sup>a</sup> Center for Orthopaedic Biomechanics, University of Denver, Denver, CO, 80208, USA

### ARTICLE INFO

**Keywords:**

Total knee arthroplasty  
Micromotion  
Cementless implant  
Finite element  
Validation

### ABSTRACT

The initial fixation of cementless tibial trays after total knee arthroplasty is crucial to bony ingrowth onto the porous surface of the implants, as micromotion magnitudes exceeding 150  $\mu\text{m}$  may inhibit bone formations and limit fixation. Experimental measurement of the interface micromotions is still very challenging. Thus, previous studies investigated micromotions at the bone-tray interface via finite element methods, but few performed direct validation via *in vitro* cadaveric testing under physiological loading conditions. Additionally, previous models were validated by solely considering relative displacements of the marker couples placed around the tray-bone interface. In this paper, we present an experimental-computational validation framework for investigating micromotions at the tray-bone interface under physiological conditions. Three cadaveric specimens were implanted with cementless rotating-platform implants and tested under gait, deep knee bending, and stair descent loads. Corresponding subject-specific finite element models were developed and used to predict the marker (tray-bone) relative displacements and tibial surface displacements. Experimental measurements were used to validate model estimations. Subsequent sensitivity analyses were performed on implantation and friction parameters to represent model uncertainties.

The models appropriately differentiated between locations, activities, and specimens. The average root-mean-square (RMS) differences and correlations between measured marker relative displacements and predictions from the 'best-matching' models were 13.1  $\mu\text{m}$  and 0.86. RMS differences and correlations between measured surface displacements and predictions were 78.9  $\mu\text{m}$  and 0.84. Full-field interface micromotions were investigated and compared with predicted marker relative displacements. The marker relative displacements underestimated the actual interface micromotions. Initial tray-bone alignment in anterior-posterior, flexion-extension, and varus-valgus degrees of freedom have a considerable impact on the interface micromotions. The validated cadaveric models can be further used for pre-clinical assessments of new TKR tray design. The outcomes of the sensitivity analyses provide further insights into reducing interface micromotions via clinical techniques.

### 1. Introduction

Cemented and cementless fixation in total knee arthroplasty (TKA) have been successfully used for decades. As the number of younger and more active patients treated with TKA continues to increase (Kurtz et al., 2009), long-term implant survivorship is of increasing importance. Although there is no significant difference in the performance and longevity between cemented and cementless fixation in TKA (Newman et al., 2018), current innovations in cementless tibial trays offer a more

long-lasting biological fixation potential (Dalury, 2016). The primary fixation of cementless tibial trays after TKA is crucial to bony ingrowth onto the porous surface of the implant (Bragdon et al., 1996) as micromotions exceeding 150  $\mu\text{m}$  may inhibit the bone formation and limit fixation (Pilliar et al., 1986). Therefore, understanding the micromotion at the tray-bone interface is critical for pre-clinical evaluations of new implant designs.

Previous studies investigated *in-vitro* micromotion between tray and bone by comparing the measured subsidence or liftoff of the baseplate

\* Corresponding author. Room 427, 2155 E. Wesley Ave., Denver, CO, 80208, USA.

E-mail address: [paul.rullkoetter@du.edu](mailto:paul.rullkoetter@du.edu) (P.J. Rullkoetter).

(measured using linear variable differential transformers) with the critical micromotion magnitude for bone ingrowth (Kraemer et al., 1995; Bhimji and Meneghini, 2012; Bhimji and Meneghini, 2014; Crook et al., 2017). However, these measurements are limited to a few distinct points at the interface, which may not correspond to actual interface micromotions in terms of magnitude and trend. Also, the micromotion contour map across the interface is not fully known. Experimental measurement of the micromotion at the tray-bone interface requires advanced imaging hardware and protocols (Camine et al., 2016). Thus, finite element (FE) models have been commonly used to estimate the interface micromotion. Computational models can complement experiments where data is difficult or impossible to measure. Once the models are validated, they can be further used for detailed analyses. There are a limited number of studies focusing on tray micromotions in cementless TKA which included validated FE models to evaluate the interface micromotion. One study developed and validated FE models from cadaveric tests to evaluate the tray-bone interface micromotion (Chong et al., 2010). However, only peak loads during gait were considered, which cannot fully account for the varying loads throughout the gait cycle. Also, the loading conditions tested in the previous studies mainly included a single vertical load (Hashemi and Shirazi-Adl, 2000; Crook et al., 2017; Yoshii et al., 1992) or a single daily activity (Bhimji and Meneghini, 2014; Yildirim et al., 2016). A recent study presented validated computational models for predicting the cementless TKA micro-motions in synthetic foam bones over a range of simulated activities of daily life (Navacchia et al., 2018). While synthetic bones (Yildirim et al., 2016; Crook et al., 2017) are preferred for the low cost and easy implantation procedures, cadaveric bones have real and heterogeneous material property distributions which reflect anatomical location and subject-specific factors. Thus, cadaveric tests provide more realistic biological fixation and enable more physiological investigation of the interface micromotion.

To our knowledge, no study has reported validated interface micromotion data (measured in cadaveric specimens implanted with the cementless trays) by considering physiological loading conditions covering multiple dynamic activities of daily living. Additionally, the majority of the previous investigations did not present detailed validation results (Chong et al., 2010) or evaluated interface micromotions without model validations (Taylor et al., 2012). Previous studies validated their FE models by solely considering relative displacements of the marker couples placed around the tray-bone interface. However, these location-specific comparisons may not reflect the validity of the entire model, particularly for cadaveric bones which possess heterogeneous material properties. The validation procedure can be improved by also considering bone surface displacements. Furthermore, previous studies only considered the fixed-bearing design for knee prostheses. Interface micromotions for the rotating platform (RP) design in cementless TKA have not been previously studied.

Hence, the objective of this work was to present a validated experimental-computational framework for predicting tibial micro-motion and bone deformation during activities of daily living. Three cadaveric tibiae were implanted with an RP cementless TKA design and were tested via a six-degree-of-freedom (DoF) knee testing machine under gait (GT), deep knee bending (DKB) and stair descent (SD) loading conditions. Relative motions between the marker couples on tray-bone exposed surfaces and anterior tibial surface displacements were measured and compared with the FE predictions.

## 2. Methods

In this study, three cadaveric tibiae were implanted and experimentally tested under physiological loading conditions. Tray-bone relative displacements and the bone surface displacements were recorded at the anterior aspects of the implanted tibiae. The corresponding computational models were developed with all the boundary conditions (implantation alignment, bone fixation, loading condition, and marker

couple location, etc.) reproduced from the experiments. The experimental measurements were compared with the predictions for validating the computational models. After validation, the tray-bone interface micromotions were investigated in detail.

### 2.1. Experimental testing

CT scans of three fresh-frozen healthy cadaveric tibiae were taken prior to the experiments and were manually segmented using ScanIP (Simpleware, Exeter, UK) from the CT scans. (Table 1). The scan parameters were set at 130 kVp, 107 mA tube current, 0.6-mm thickness slices, and 0.39-mm pixel spacing with a scan field of 200 mm. Each specimen was implanted using mechanical alignment techniques with a cementless tibial prosthesis (best-fit size, rotation-platform, cruciate-retaining, ATTUNE®, Depuy Synthes, Warsaw, IN) by an experienced surgeon. The specimen was resected 12.7 cm distal from the implantation plane. Good fixation support and sufficient coverage were noted for all the specimens. After the implantation, specimens were cemented into custom fixtures (Fig. 1). Nine digital image correlation (DIC) target markers were then placed at the anterior aspects of the tray and the bone, respectively. Three markers were additionally placed on the fixture to generate a local coordinate system. A speckle pattern was applied on the anterior surface of the tibia to enable measuring surface displacements. The tray and tibia surfaces were probed using the OPTOTRACK® system (NDI, Waterloo, Ontario) to reproduce the same tray-bone alignment for the FE models. Subsequently, the specimens were mounted into the 6-DoFs AMTI VIVO™ knee simulator (AMTI, Watertown, MA) and were tested under simulated gait (GT), deep-knee bending (DKB), and stair descent (SD) activities. Experimentally applied load and kinematics profiles were derived from telemetric implant data and ASTM 3141-17 (Navacchia et al., 2018). Flexion/extension and internal/external rotation (IE) degrees of freedom (DoFs) were kinematically-driven while medial/lateral (ML), anterior/posterior (AP), superior/inferior (SI), and varus/valgus (VV) DoFs were load controlled. After bedding-in under cyclic compression for 200 cycles, 40 cycles of each activity were performed at a rate of 0.33 Hz. Relative displacements between the corresponding tray-bone marker couples and tibial surface displacements in the local coordinate system were recorded with the ARAMIS DIC system (GOM mbH, Braunschweig, DE) for the 36<sup>th</sup>–39<sup>th</sup> cycles (Fig. 2). Reference images were captured at the unloaded stage before each tested activity to set the displacements to zero and thus ignore any plastic deformation created previously.

#### 2.1.1. Loading and boundary conditions

The desired experimental load and kinematics profiles (Fig. 3) input to the VIVO were usually slightly different from the actual outputs. Hence, the output load and kinematics profiles were recorded for each actuator in the VIVO device and later applied to the finite element models.

### 2.2. Computational modeling

#### 2.2.1. Model set up

The position and orientations of the tray and tibia in the experimental set up were reconstructed by registering measured point clouds to respective stereolithography geometry files (Fig. 1). For this, the iterative closest point algorithm was used, and the root-mean-square (RMS) error of registration was less than 1 mm for both components.

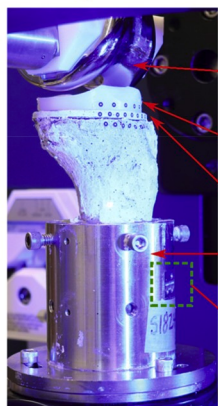
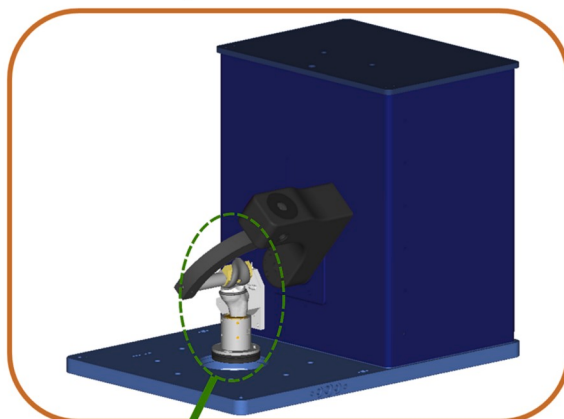
**Table 1**  
Specimen information and implantation sizes.

Specimen	Age	Gender	Height (cm)	Left/Right	Implanted tray size
1	53	F	160	Left	5
2	75	F	157.5	Right	4
3	70	F	157.5	Right	5

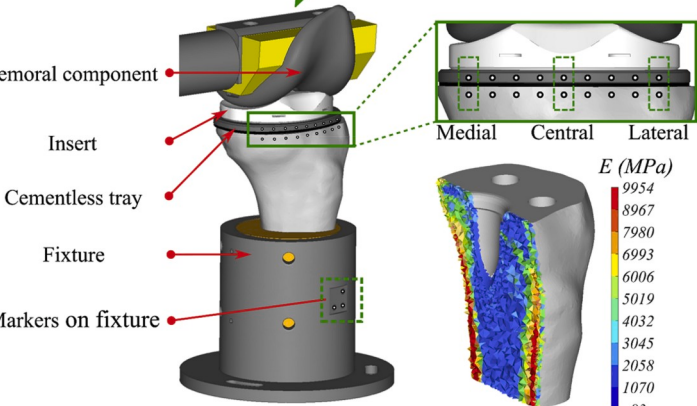
## Experimental framework



## Computational framework

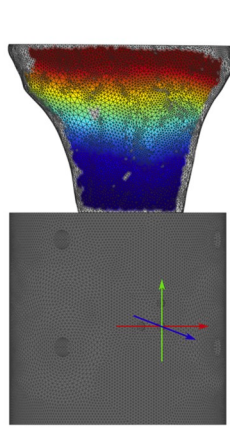
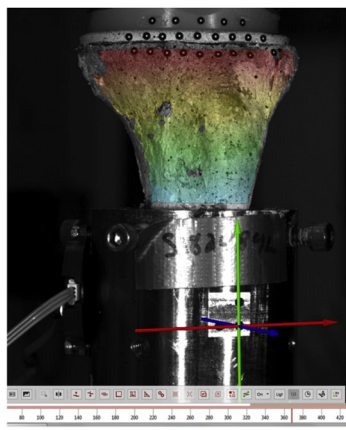


(a)



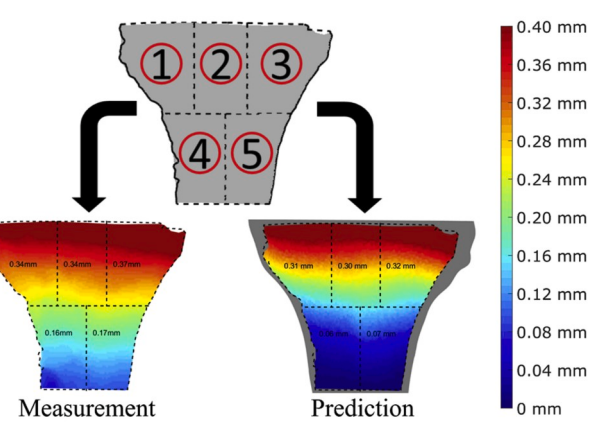
(b)

**Fig. 1.** (a) Experimental set up with one of the specimens (left knee). (b) The corresponding finite element representation. Highlighted three marker couples (medial, central, and lateral) were used to measure and predict the relative displacement between the tray and tibia. A section view of the tibia with Young's modulus assigned from the CT scans.



(a)

(b)



(c)

**Fig. 2.** (a) Illustration of the anterior tibial surface displacement for one of the specimens (left knee). The fixture-local coordinate system definition is also shown. (b) The corresponding finite element representation. The experimentally captured surface was isolated from the model. (c) Tibial surface was divided into five regions for comparing measured and predicted displacements. Average displacements were calculated within the regions.

The positions of the DIC marker couples were also reproduced during the registration process.

The prosthesis was virtually implanted, and the portion of the distal tibia confined to the fixture was resected in HyperMesh (Altair

Engineering Inc., Troy, Michigan). The tray was modeled with a solid portion and a porous coating (represented also as a solid) according to real dimensions. The femoral component was meshed with 1-mm rigid surface elements. The deformable TKA components were meshed with

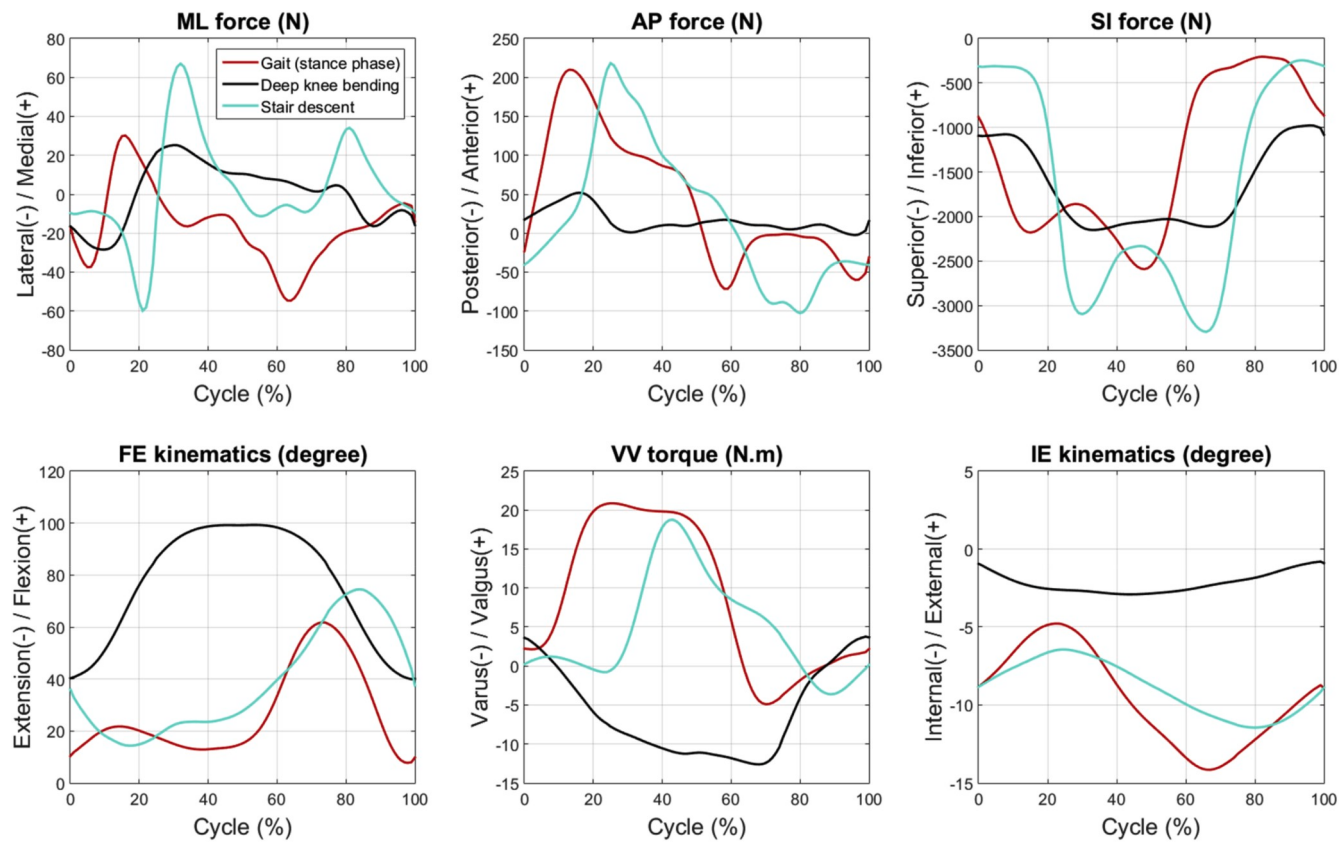


**Fig. 3.** The load and kinematics profiles applied to VIVO actuators for a left knee. The flexion/extension kinematics and varus/valgus torque were applied to the femoral component via the upper stage of the VIVO. The medial/lateral, anterior/posterior, superior/inferior forces, and internal/external kinematics were applied to the implanted tibia via the lower stage.

0.5 mm, first-order, tetrahedral elements, except the solid portion of the tray which was discretized with 1.0 mm elements. The applied mesh sizes were sufficiently fine for convergence (Halloran et al., 2005). The tibia was meshed with first-order, tetrahedral elements, and the most efficient mesh density was identified from our mesh convergence study (0.75 mm at the coating-bone interface, 1.5 mm on the surface, 3 mm inside the bone; see section 3.1 for the result of this convergence study). All components were modeled as linearly elastic and with different material properties, except the insert which was modeled with an elastic-plastic hardening material property (Table 2).

Specimen-specific material properties were calculated from the CT scans and were assigned to each tibias element by using an in-house developed, mapping software. The relation between the Hounsfield unit and bone mineral density was derived using a calibration phantom (QCT Pro, Mindways Software, Inc., Austin TX). Previously established relationships were used for calculating the apparent bone density and elastic modulus for the individual elements (Kaneko et al., 2004; Linde et al., 1991; Anderson et al., 1992). A threshold value of 1 g/cm<sup>3</sup> for apparent bone density was used for discriminating cortical bone from

trabecular bone. Approximately 400 material cards (1 card per 4 mg/cm<sup>3</sup> bone apparent density) were used for modeling the tibiae based on our convergence study (see section 3.1 for the result of this convergence study).

Finite element models of the tested specimens were developed in Abaqus/Standard (SIMULIA, Providence, RI). The interaction between the tibia and the coating was defined with friction ( $\mu_d = 1.00$ ) as measured in a previous study (Navacchia et al., 2018). The coating was tied to the solid portion of the tray. The contacts between the polyethylene and metal components (insert-tray and insert-femoral) were modeled with friction ( $\mu_d = 0.04$ , Godest et al., 2002). All the contacts were defined as contact pairs with a smooth surface-to-surface contact. We chose the master surfaces to have higher stiffness and the slave surfaces to have lower stiffness. Also, master surfaces had the same or coarser mesh compared to the slave surfaces. Interference fit was not considered in the FE simulations. However, the impact of the interference fit was assessed.

The implant-bone construct was virtually mounted into the VIVO simulator model (Fitzpatrick et al., 2016) and loaded via a femoral

**Table 2**

Material properties used in the computational models. Transversely isotropic material properties were defined for the porous coating according to internal experimental data. Z-direction is perpendicular to the porous surface.

Material	Density (g/cm <sup>3</sup> )	Elastic moduli (MPa)			Yield stress (MPa)	Poisson's ratios		
		E <sub>x</sub>	E <sub>y</sub>	E <sub>z</sub>		ν <sub>xy</sub>	ν <sub>yz</sub>	ν <sub>xz</sub>
Insert - UHMWPE	0.94	571.6			8.1	0.45		
Tray solid - CoCrMo	8.50	220,000			–	0.3		
Tray porous - CoCrMo	0.05	700	700	2200	–	0.083	0.083	0.083
Cortical bone	≥1	≤9954			–	0.3		
Trabecular bone	≤1	≥79.6			–	0.3		

component with the boundary conditions derived from the VIVO. The distal end of the tibia was rigidly fixed to the fixture to efficiently represent the cemented bone-fixture fixation. Two cycles were simulated for each activity based on our convergence study which identified the minimum number of cycles required to reach a steady state (see section 3.1 for the result of this convergence study).

### 2.2.2. Model verification and sensitivity

A number of convergence studies were investigated on key modeling factors to verify the predictions of the computational model. The edge lengths of the tibial elements were analyzed with (0.75 and 1.5) mm (tray-bone interface and remaining surface), (1.0 and 2.0) mm and (2.0 and 4.0) mm. For defining material properties of the tibia, 100, 200, 300, and 400 material cards were considered. Tibial elements were grouped into element sets by elastic modulus and density properties. Since the finite element model was mostly load driven, the kinematics paths could change between each simulated cycle. Therefore, ten cycles were continuously simulated and investigated the model convergence. An interference fit of 2, 5, 10, 25, 50, and 100  $\mu\text{m}$  was applied to the pegs at the bottom of the porous coating. The maximum interference fit of 100  $\mu\text{m}$  was considered according to the reported threshold value which is safe against bone fracture (Abdul-Kadir et al., 2008).

Sensitivities of the computational predictions were also investigated to include the potential errors in geometric representation and contact properties. Investigated parameters were applied to the baseline model (the initial model developed from the experiment) and were as follow:

- **Tray-bone alignment:** Twelve models were developed by perturbing tray-bone alignment (considering one perturbation at a time):  $\pm 0.5$  mm in anterior-posterior (AP),  $\pm 0.5$  mm in medial-lateral (ML), and  $\pm 0.25$  mm translation in superior-inferior (SI), and  $\pm 0.25^\circ$  in tibial slope,  $\pm 0.25^\circ$  in varus-valgus (VV), and  $\pm 1^\circ$  rotation in internal-external (IE).
- **Tibia marker locations:** For each marker (re-constructed during the registration step), twelve nearest nodes on the tibia surface were selected. Thus, each tray-bone marker couple had twelve possible configurations. The distances between each possible marker (node) and the initial marker location were less than 1 mm.
- **The coefficient of friction:** The mean coefficient of friction was defined as 1.00 at the tray-bone interface based on test data from the manufacturer, and the coefficient of friction was perturbed in a range of 0.80–1.20 to represent the experimental variability.

All verification and sensitivity study parameters were firstly investigated on the first specimen for the gait activity. The impact of each sensitivity parameter on the bone-implant relative displacements was identified. Subsequently, upper and lower-bound model configurations were developed from all the sensitivity parameters. The developed upper and lower bound configurations were later applied to all the specimens to study GT, DKB and SD activities.

### 2.3. Data analysis

#### 2.3.1. Marker relative displacements

For each activity of all the specimens, the predicted and measured relative displacements of the medial, central, and lateral marker couples were compared. Thirty-six results (the baseline, upper and lower-bound model configurations with 12 marker pair configurations) characterized the uncertainty bounds for each marker. The average root-mean-square (RMS) differences between measured and predicted marker relative displacements and Pearson's correlations were calculated to evaluate the overall performance of the computational models. The configuration with the lowest RMS difference (considering medial, central, and lateral markers concurrently) was identified as the 'best-matching' model. Similarly, the configuration with the largest RMS difference was identified as the 'worst-case' model. The Pearson's correlations between the

predictions of the best matching models and the corresponding experimental measurements (*intra*-activity correlation) were also calculated. In addition, the correlations between the same predictions and the measurements from the other two activities (*inter*-activity correlations) were calculated to assess if the models might distinguish between activities.

#### 2.3.2. Tibial surface displacements

For each activity, the anterior surface displacement of the tibiae captured by the DIC system was re-constructed in the computational model. The average differences between predicted and measured tibial surface displacements were calculated. The surface displacements at 30%, 50% and 70% of the activity cycle were graphically compared. The anterior surface of the tibia was divided into five regions, and the average displacement within each region was calculated for every 1% of the activity cycle (Fig. 2). The Correlation between the predicted and measured surface displacements for these regions was calculated and visualized graphically by creating a scatter plot and applying linear regression. Similar to relative marker displacements, the *inter*- and *intra*-activity correlations were also calculated.

We defined the tibial regions illustrated in Fig. 2 as follows. The captured tibia surface was firstly divided into superior (regions 1–3) and inferior (regions 4–5) parts having the same height. The regions in the superior (three regions) and inferior (two regions) parts were then constructed to have approximately equal areas in the corresponding parts.

#### 2.3.3. Tray-bone interface micromotions

In this study, we defined the tray-bone interface micromotion as the relative motions between the tray and the tibia contact surface. In computational models, the changes in the relative distance (total of the three translational components) between the nodes at the tray bottom surface and the nearest nodes at the tibia implantation surface were used to represent the tray-bone interface micromotion. For each activity, the micromotion at the tray-bone interface was predicted. The micromotion contour map for the frame having the peak micromotion was also presented. The maximum values of the interface micromotions through the entire activity cycle were compared to the predicted marker relative displacements to assess if the marker relative displacements can represent actual interface micromotions. The Pearson correlations and maximum differences between these two features were also calculated. The maximum values of the interface micromotion predictions from the baseline, upper and lower-bound models were also compared.

### 3. Results

In this section, the findings from the convergence and sensitivity studies are presented first as these dictated some model parameters. We then compared experimentally measured marker relative and bone surface displacements to computational predictions for validating the developed models. Subsequently, interface micromotions predicted by the validated computer models are reported.

#### 3.1. Model setup and sensitivity

##### 3.1.1. Mesh convergence study

The RMS differences between the predicted marker relative displacements when using 0.75 and 1.0 mm mesh sizes were 1.39, 2.57, and 1.15  $\mu\text{m}$  (medial, central, and lateral). These differences were on average 0.8% of the relative displacement ranges. The maximum difference between the tibial surface displacements with the two mesh sizes was 19.4  $\mu\text{m}$  (2.2% of the maximum displacement). Based on these mesh evaluations, 1.0 mm was considered acceptable for further analyses.

##### 3.1.2. Number of materials to represent tibial bone

The average RMS difference between the marker relative

displacements estimated with 100 and 400 material cards were 1.15, 1.09, and 0.86  $\mu\text{m}$  (medial, central, and lateral), which were on average 0.5% of the relative displacement ranges. The maximum difference between the tibial surface displacements was 11.5  $\mu\text{m}$  (1.3%).

### 3.1.3. Number of activity loading cycles represented

The maximum marker relative displacement and maximum surface displacement predicted from the first simulated cycle were 141.6  $\mu\text{m}$  (68.8%) and 235  $\mu\text{m}$  (26.6%) smaller than the predictions from the 2nd cycle. The maximum differences between the marker relative displacements predicted from the 2nd cycle and any subsequent cycle were 1.23, 1.50, and 1.90  $\mu\text{m}$  (medial, central, and lateral), which were on average 0.7% of the relative displacement ranges. The maximum difference between the tibial surface displacements was 29.2  $\mu\text{m}$  (3.3%).

### 3.1.4. Line-to-line vs. interference fit for tray in bone

The maximum interface micromotion predicted by applying 100  $\mu\text{m}$  interference fit was 33.0  $\mu\text{m}$  (15.9%) reduced comparing with the prediction without interference fit (Fig. 4). The maximum difference between the tibial surface displacements was 43.3  $\mu\text{m}$  (4.9%).

### 3.1.5. Impact of tray alignment

The results of the sensitivity analyses are shown in Fig. 5. Perturbations of the tray alignment in AP and tibial slope directions resulted in 8.78% and 5.05% changes in marker relative displacement ranges. Average changes caused by perturbations along ML (3.22%), SI (3.76%), VV (1.94%), and IE (0.77%) directions and in friction coefficient (1.04%) were much smaller. Percent differences in tibial surface displacements were always less than 5% (for all perturbed parameters).

## 3.2. Marker relative displacements

Measured and predicted marker relative displacements for the three specimens were compared in Fig. 6 and Table 3. The RMS differences and Pearson's correlations between the measured and predicted values were shown. The RMS differences between the measurements and predictions (from the 'best-matching' models) were (16.4, 5.7, 13.0)  $\mu\text{m}$  (GT, DKB, and SD), (15.9, 7.7, 22.3)  $\mu\text{m}$ , and (12.3, 8.7, 6.6)  $\mu\text{m}$  for specimens 1, 2, and 3, respectively. The corresponding correlations were (0.94, 0.88, 0.96), (0.96, 0.95, 0.88), and (0.91, 0.84, 0.93) on average. The *intra*-activity correlations were consistently higher than *inter*-activity correlations for all three specimens (Table 4). The RMS differences

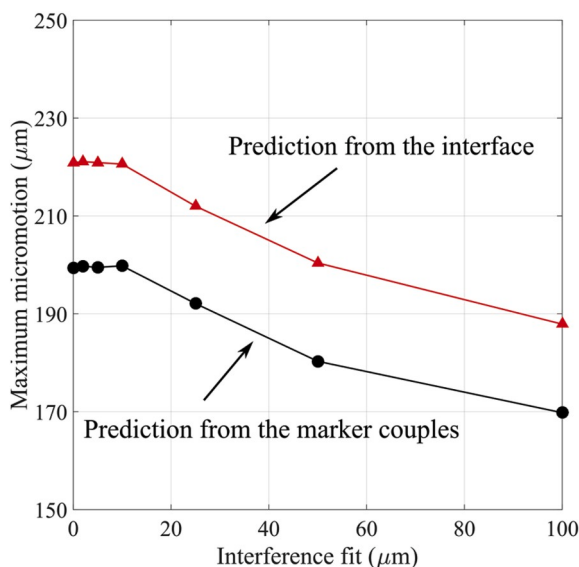


Fig. 4. The impact of the interference fit on tray-bone micromotion predictions.

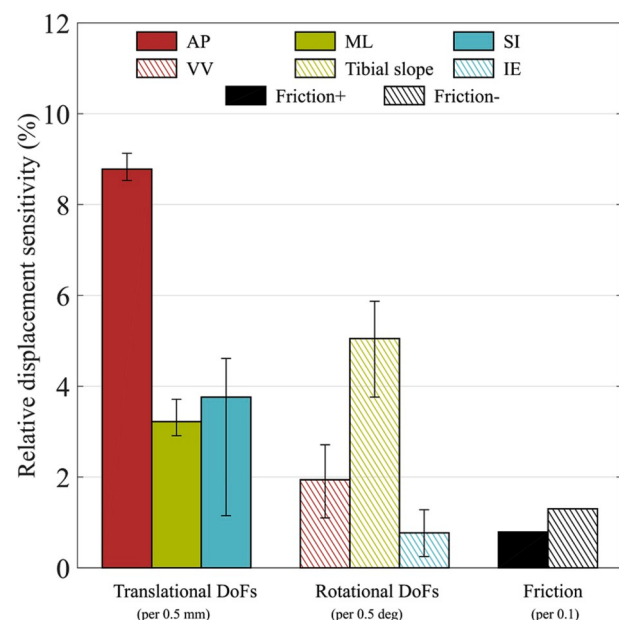


Fig. 5. The percent changes in marker relative displacement ranges due to perturbed sensitivity parameters. (Friction  $\pm$  indicates an increase or decrease from the nominal coefficient of friction,  $\mu = 1.00$ ).

between the measurements and the predictions from the 'worst-case' models were (33.7, 13.6, 47.5)  $\mu\text{m}$  (GT, DKB, and SD), (35.5, 35.2, 48.7)  $\mu\text{m}$ , and (21.9, 17.1, 23.2)  $\mu\text{m}$  for specimens 1, 2, and 3, respectively. The average difference between the 'best-matching' and the 'worst-case' models was 25.8  $\mu\text{m}$ .

## 3.3. Tibial surface displacements

Since the predictions of tibial surface displacements were not as sensitive to perturbed parameters, only the results from the baseline models were presented in this section. Measured and predicted full-field surface displacements at 30%, 50%, and 70% of the activity cycles are shown in Fig. 7. The average differences between predicted and measured surface displacements over the entire activities were (13.07%, 10.90%, 6.87%) (GT, DKB, and SD), (10.05%, 8.09%, 5.68%), and (8.34%, 13.44%, 4.76%) for specimens 1, 2, and 3, respectively. The correlations and average RMS differences between predictions and measurements are shown in Fig. 8. The *intra*-activity correlations were consistently higher than *inter*-activity correlations, except for the second specimen in DKB (Table 5).

## 3.4. Tray-bone interface micromotions

The micromotion contour maps at the frames having the peak micromotions were predicted by using the baseline models (Fig. 9). Peak micromotions were observed at the anterior tray-bone interfaces for all the specimens in each activity, except for the third specimen in DKB, for which almost no micromotion was found at the anterior side. This finding was in agreement with the experimental data (Fig. 6, specimen 3, DKB) which showed non-positive relative displacements at the anterior side. The correlations between maximum values of the interface micromotions and the marker relative displacements through entire activity cycles were (0.94, 0.22, 0.89) (GT, DKB, and SD), (0.99, 0.93, 0.98), and (0.85, 0.47, 0.89) for specimens 1, 2, and 3, respectively. The maximum values of the predicted interface micromotions were consistently higher than the maximum marker relative displacements (Fig. 10). The maximum differences between these two features were (17.8, 28.3, 26.7)  $\mu\text{m}$  (GT, DKB, and SD), (6.3, 24.5, 11.7)  $\mu\text{m}$ , and (6.3, 25.7, 10.4)  $\mu\text{m}$  for specimens 1, 2, and 3, respectively. The maximum

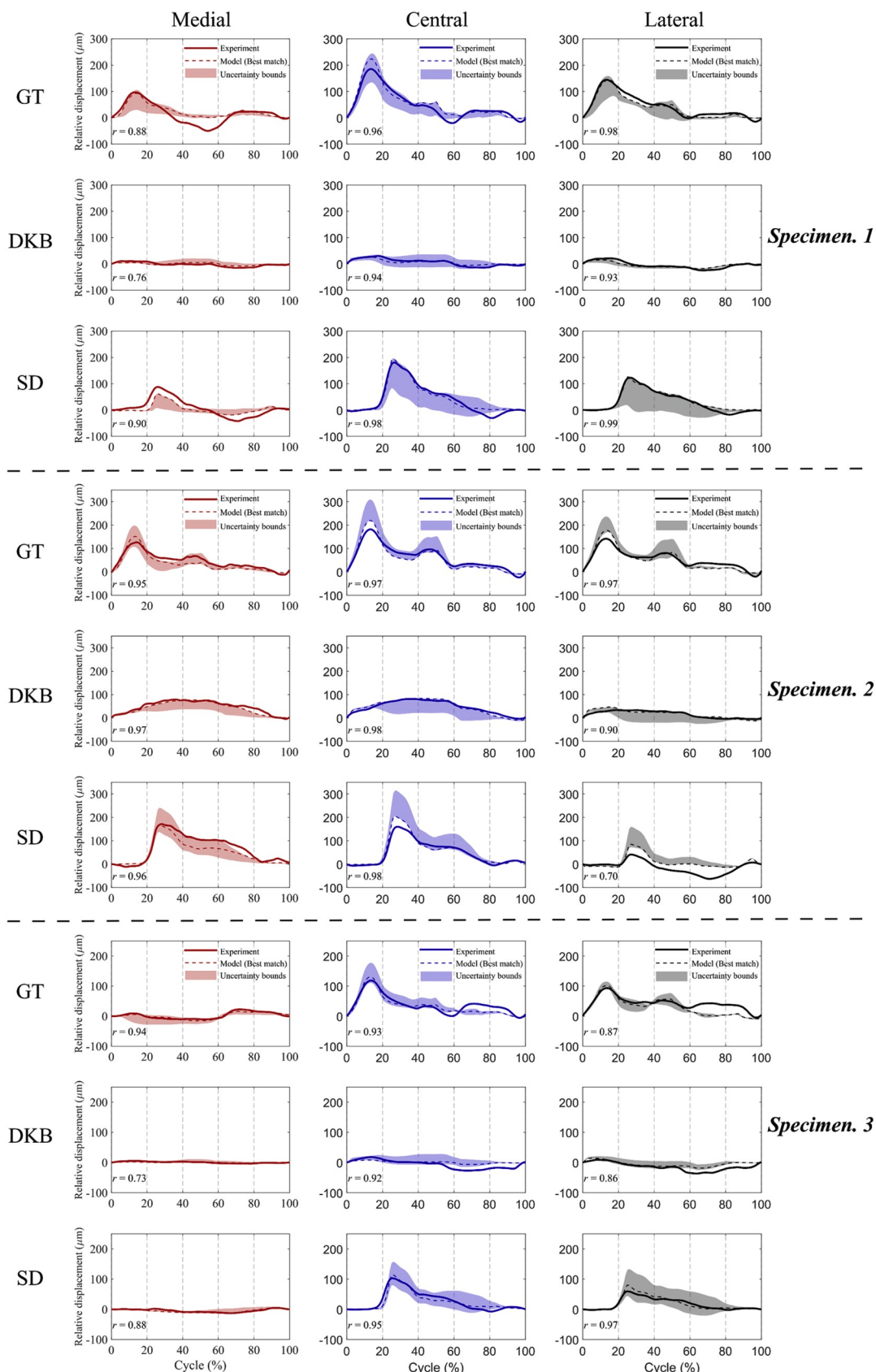


**Fig. 6.** Comparison between measured (solid lines) marker relative displacements and the predictions from the ‘best-matching’ models (dashed lines). Uncertainty bounds (shaded areas) were generated by perturbing implantation parameters and friction coefficients.

**Table 3**

Specimen 1											
RMS differences ( $\mu\text{m}$ )											
Medial		Central		Lateral		Pearson's Correlations					
Best match	Average	Best match	Average	Best match	Average	Best match	Average	Best match	Average	Best match	Average
GT	<b>21.81</b>	26.67	<b>17.17</b>	18.17	<b>10.27</b>	20.20	GT	<b>0.88</b>	0.82	<b>0.96</b>	0.96
DKB	<b>5.42</b>	8.37	<b>5.85</b>	10.27	<b>5.94</b>	7.84	DKB	<b>0.76</b>	0.53	<b>0.94</b>	0.81
SD	<b>19.01</b>	27.48	<b>12.40</b>	31.92	<b>7.62</b>	30.86	SD	<b>0.90</b>	0.74	<b>0.98</b>	0.94

Specimen 2											
RMS differences ( $\mu\text{m}$ )											
Medial		Central		Lateral		Pearson's Correlations					
Best match	Average	Best match	Average	Best match	Average	Best match	Average	Best match	Average	Best match	Average
GT	<b>16.19</b>	19.17	<b>15.97</b>	27.57	<b>15.48</b>	25.29	GT	<b>0.95</b>	0.93	<b>0.97</b>	0.97
DKB	<b>8.60</b>	19.61	<b>6.78</b>	21.42	<b>7.71</b>	19.60	DKB	<b>0.97</b>	0.92	<b>0.98</b>	0.84
SD	<b>23.79</b>	29.25	<b>14.18</b>	33.37	<b>28.83</b>	41.35	SD	<b>0.96</b>	0.93	<b>0.98</b>	0.98

Specimen 3											
RMS differences ( $\mu\text{m}$ )											
Medial		Central		Lateral		Pearson's Correlations					
Best match	Average	Best match	Average	Best match	Average	Best match	Average	Best match	Average	Best match	Average
GT	<b>3.89</b>	7.42	<b>13.21</b>	16.48	<b>19.77</b>	20.96	GT	<b>0.94</b>	0.91	<b>0.93</b>	0.91
DKB	<b>2.09</b>	3.17	<b>12.54</b>	15.14	<b>11.58</b>	13.50	DKB	<b>0.73</b>	0.44	<b>0.92</b>	0.80
SD	<b>3.06</b>	4.12	<b>10.06</b>	17.95	<b>6.75</b>	16.80	SD	<b>0.88</b>	0.68	<b>0.95</b>	0.93

**Table 4**

Intra (highlighted in bold) and inter-activity (values outside the diagonal) correlations between the measured marker relative displacements and predictions from the 'best-matching' models.

Specimen 1			Specimen 2			Specimen 3			
	Exp. GT	Exp. DKB	Exp. SD	Exp. GT	Exp. DKB	Exp. SD	Exp. GT	Exp. DKB	Exp. SD
Model GT r	0.94	0.40	0.23	0.96	0.63	0.08	0.91	0.08	0.17
Model DKB r	0.71	0.88	0.14	0.42	0.95	0.65	0.30	0.84	0.14
Model SD r	0.24	0.04	0.96	0.01	0.64	0.88	0.19	-0.02	0.93

values of the interface micromotions predicted from the upper-bound models were consistently higher than those from the baseline models for all specimens in each activity (Table 6). On the contrary, the lower-bound models presented consistently lower interface micromotions than the baseline models. Also, interface micromotion and predicted marker couple relative displacements were the highest in gait followed by stair descent, and deep-knee bending activities.

#### 4. Discussion

A fundamental step in the design of cementless TKR prostheses is to assess their performance under physiological loading conditions. Cadaveric tests are essential since real bone has heterogeneous material property distributions which reproduce real contact conditions. Current in-vitro experimental platforms enable applying physiological loadings in 6-DoFs and measuring micro-level displacements. However, it is usually not feasible to fully measure the micromotion at the implant-bone interface, which is a critical parameter for evaluating the primary fixation. Also, cadaveric specimens are unique and non-reusable after testing. The test conditions applied to one specimen cannot be perfectly replicated when testing other specimens. When studying the impact of a specific factor, the experimental method usually requires a large number of specimens to obtain statistically significant differences, which will highly increase the costs. Validated computational models can address these limitations and enable investigating implant-bone interface micromotion in detail and more robustly. Desired loading conditions can be tested with the validated models for further studies, even if those loading conditions cannot be tested experimentally. Validated models can be further used to isolate and study the impact of different surgical and patient factors, which are difficult or impossible by only using experimental setups. Consequently, the validation of computational models is crucial to further understand cementless fixation via computational methods.

This study presented a detailed computational-experimental validation framework for investigating implant-bone interface micromotions.

In this study, three cadaveric specimens were implanted with cementless, rotating-platform TKR components and were tested under physiological loading conditions. Subject-specific finite element models were developed and used to predict marker relative and tibial surface displacements. Experimental measurements were performed and used to validate model predictions. For all the specimens, different ranges of medial, central, and lateral marker relative displacements were correctly predicted (Fig. 6), which indicated that developed models distinguished between different locations. Presented significantly higher intra-activity correlations (than the inter-activity correlations, Table 4) demonstrates that the models were able to distinguish between different activities. For each specimen, different trends and ranges of marker relative displacements were measured and captured by the predictions, which pointed out that the models also differentiated between the specimens. The models also computed characteristic tibial surface displacements. Predicted tibial surface displacements successfully captured magnitudes and the trends of the measurements for all the specimens in each activity (Figs. 7 and 8). The differences between intra and inter-correlations (Table 5) also verified the predictions did not share similarities between different activities. The reliability of the computational validation was improved by accurate predictions of both marker relative and bone surface displacements. Model uncertainties were considered by including the results from upper-bound and lower-bound models. Average RMS differences (for all the specimens) and correlations between the measurements and all the probabilistic results were 19.8  $\mu\text{m}$  and 0.83, while those values were 12.1  $\mu\text{m}$  and 0.92 for the 'best-matching' models. Overall, the models were successful in predicting both trend and magnitude of both marker and surface displacements using the complementary experimental-computational framework. Additionally, experimental measurements showed significant differences in trends and ranges not only between different activities but also among different specimens. Although the first and the third specimens were implanted with the same tray size, measured marker relative displacements were very distinct. These findings confirm the necessity to test real bone geometries under different loading conditions and to

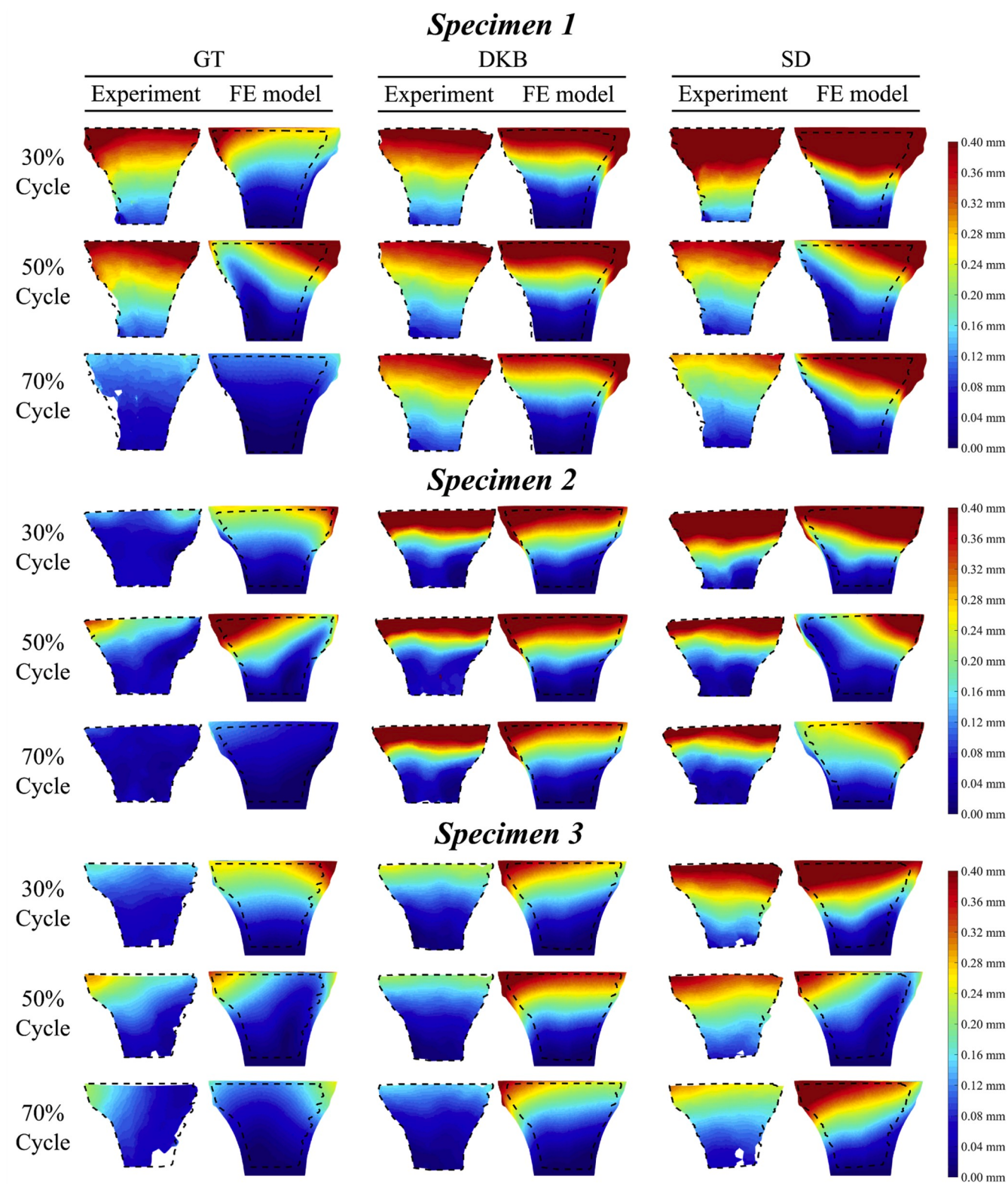


**Fig. 7.** Full-field measured and predicted surface displacements were compared at 30%, 50%, and 70% of the activity cycles.

consider populations when assessing implant primary stability.

Previous studies either lacked different continuous physiological loading conditions (Chong et al., 2010) or human bone representatives (Navacchia et al., 2018). The loading conditions obtained from AMTI VITO™ knee simulator were always applied to the femoral component (Navacchia et al., 2018), which was inconsistent with the actual

operational mechanism of the simulator (two DoFs were applied by upper stage, four by lower stage). To our knowledge, this study is the first to validate cadaveric models for predicting interface micromotions under different physiological loading conditions. The complexity of the validations was further increased by the rotating-platform implant design and including the mechanisms of the knee simulator. Studies

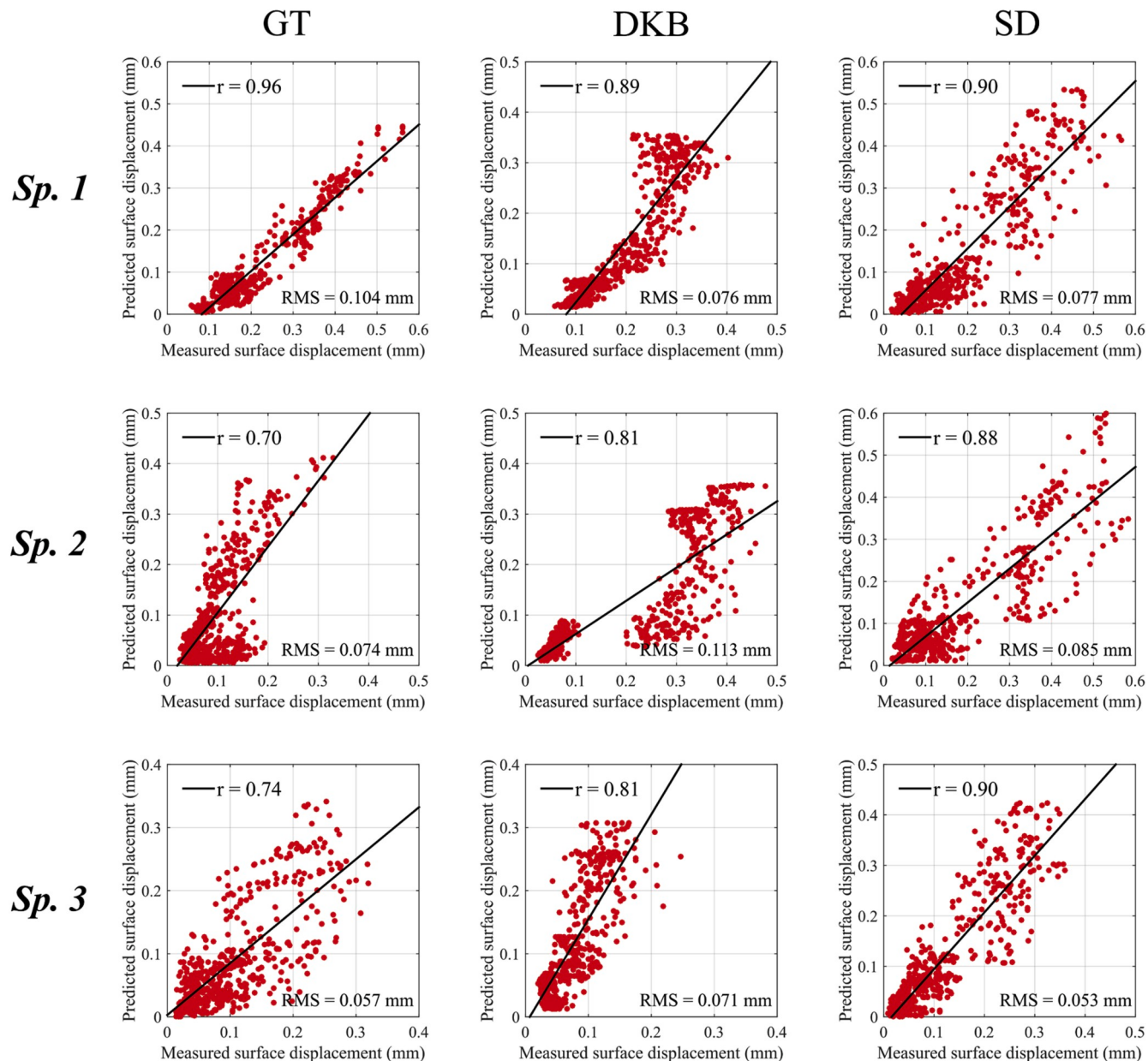


**Fig. 8.** Pearson's correlations and average RMS differences between measured and predicted surface displacements from five sub-regions are shown.

**Table 5**

*Intra* (bold) and *inter*-activity correlations between the measured surface displacements and predictions from the baseline models.

	Specimen 1			Specimen 2			Specimen 3		
	Exp. GT	Exp. DKB	Exp. SD	Exp. GT	Exp. DKB	Exp. SD	Exp. GT	Exp. DKB	Exp. SD
Model GT $r$	0.96	0.62	-0.06	0.70	0.51	0.38	0.74	0.61	0.25
Model DKB $r$	0.56	0.89	0.85	0.15	0.81	0.88	0.63	0.81	0.80
Model SD $r$	0.35	0.79	0.90	-0.05	0.58	0.88	0.42	0.65	0.90

validated finite element models by solely considering regional relative displacements, but the validity of the entire models remains uncertain. This study makes the first attempt to improve the validation process by considering both tibial surface and marker relative displacements.

This study addressed the concern that if marker relative displacements could accurately represent actual tray-bone interface micromotions, as marker displacements were directly used to assess interface micromotions in some previous studies. We found that marker relative displacements well captured the trend of actual interface micromotions

but were usually smaller in magnitudes (Fig. 10). This was mainly due to the fact that peak interface micromotions usually occurred in between the positioned marker couples (Fig. 9). These underestimations can be partially eliminated by using more markers. For example, for the third specimen in stair descent, the predicted maximum marker relative displacement increased from 116.6  $\mu\text{m}$  (8.2% lower than predicted interface micromotion) to 126.3  $\mu\text{m}$  (3.0% lower) if all nine marker couples (Fig. 1) were considered.

We also found that uncertainties in modeling parameters had

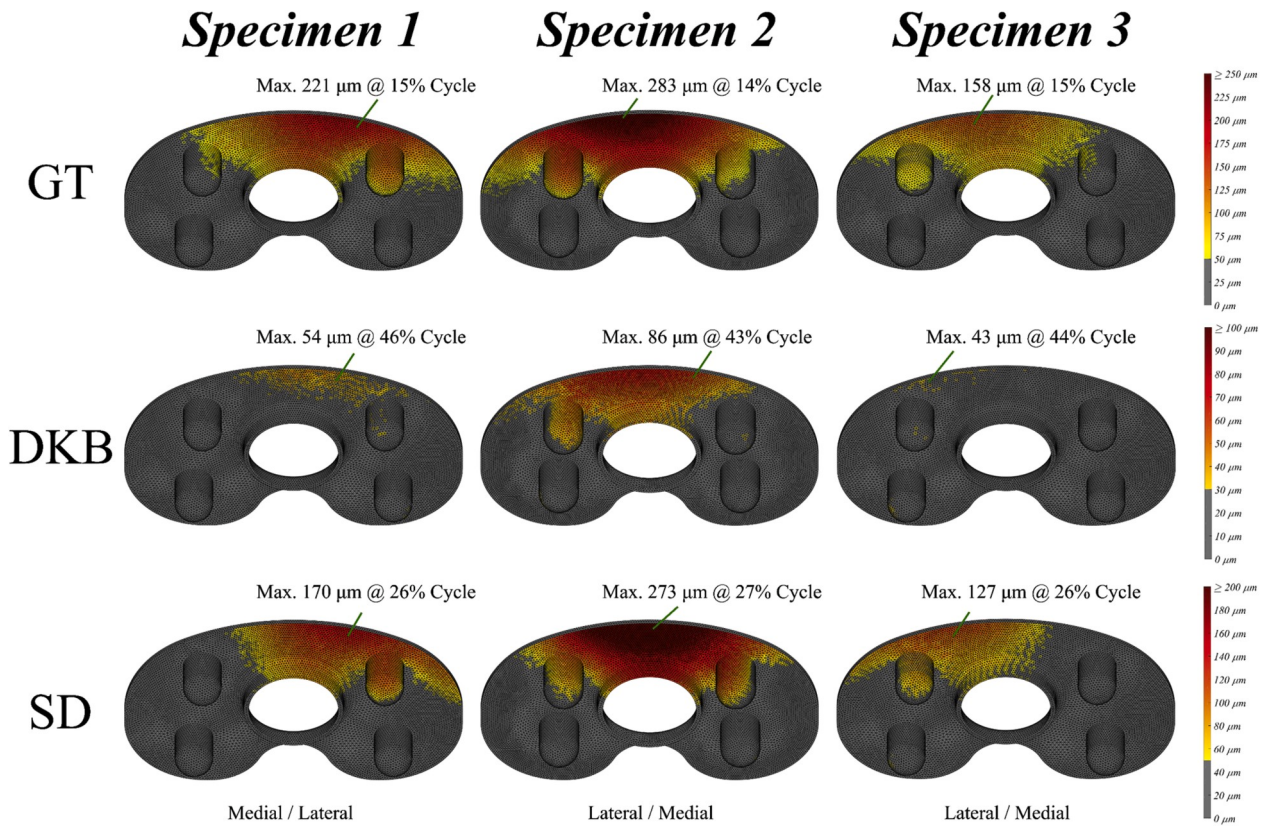


**Fig. 9.** Predicted interface micromotions at the frames having peak micromotion magnitudes. The color bar ranges were: gait activity (0–250 μm); deep knee bending activity (0–100 μm); stair descent activity (0–200 μm).

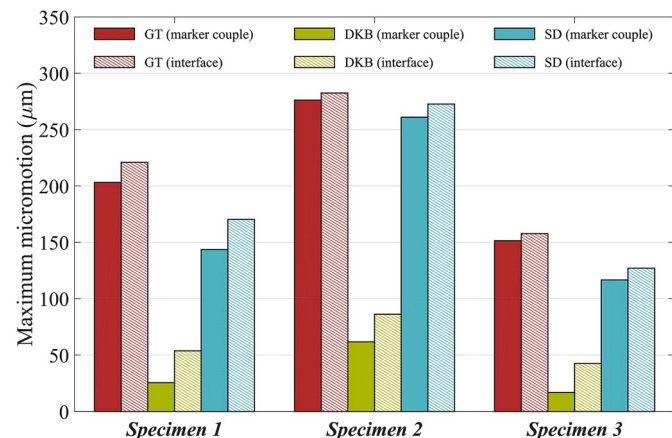


**Fig. 10.** Comparisons between maximum marker relative displacements and the maximum interface micromotions.

considerable effects on interface micromotions (Table 6). The interface micromotions predicted from the upper-bound models were on average (53.2, 21.9, 70.4) μm (GT, DKB, and SD) larger than those predictions

from the lower-bound models. This was likely due to the changes in implantation surface modulus, bone coverage, or location of tibial-bone load transfer, which were all altered after perturbations. This suggests that the interface micromotions could be partially minimized by optimizing the alignment of the tray with respect to the bone within a safe range, and that AP and tibial slope are most impactful.

The convergence study indicated that using 100 material cards for modeling the tibia material distributions was sufficient. This was in good agreement with a previous study (Zannoni et al., 1999). We chose to use around 400 material cards since this parameter did not increase the computational time and is empirically more realistic. In addition, the marker relative and surface displacements predicted from the first simulated cycle were considerably lower than the predictions from the subsequent cycles. This was in contradiction with an earlier study which found that the relative interface motion was larger in the first cycle when including the friction at the bone-implant interface Verdonck and Huiskes (1996). The reason was that the femoral-insert contact locations were not consistent at the beginning and the end for the first cycle since our models were mostly load-controlled, whereas the steady contact paths were observed in subsequent cycles. Therefore, the results from the first cycles were excluded from this study. Although the impact of interference fit on micromotion predictions was considerable (Fig. 4), the pre-stresses caused by the interference fit would reduce significantly over time due to the viscoelasticity of the human bones (Norman et al.,

**Table 6**

The maximum values of the interface micromotions (in μm) predicted from the baseline, upper-bound, and lower-bound models.

	Specimen 1			Specimen 2			Specimen 3		
	GT	DKB	SD	GT	DKB	SD	GT	DKB	SD
Baseline model	220.9	53.8	170.3	282.5	86.2	272.7	157.7	42.6	127.0
Upper-bound model	258.4	65.2	213.9	316.0	98.8	323.2	183.2	53.0	159.6
Lower-bound model	194.9	37.0	140.8	256.5	75.4	237.2	146.6	39.0	107.6

2006). A previous study (Shultz et al., 2006) estimated the relaxation was approximately 50%. In this case, the impact of interference fit would be less than 10.0% in the presented models.

Limitations of this study should be noted. Firstly, rigid bone-fixture fixation was assumed in the computational models. The cement medium inside the fixture was not modeled directly. Non-zero displacements measured at the distal fixation end for the first specimen in all activities (Fig. 7) indicated that the cement was deformed or not leveled at the fixation level. We believe including a deformable cement component would improve predictions of the surface displacements. Only one density-elasticity relationship was considered for the tibiae specimens. A previous study discussed that each bone specimen could have a characteristic density-elasticity relationship (Eberle et al., 2013). Lastly, the sensitivity parameters making the upper and lower-bound configurations were developed only from the gait activity. These upper and lower-bound configurations were then directly applied in deep knee bending and stair descent activities. Nevertheless, marker relative displacements (Fig. 6) and interface micromotions (Table 6) indicated that this was a reasonable approach for studying both activities.

In conclusion, this study presented a validated experimental-computational framework (based on cadaveric tests under physiological loading conditions) for investigating micromotions at the cementless tray-bone interface. The reliability of the validations was improved by both considering marker relative displacements and surface displacements. The models differentiated between different locations, activities, and specimens. Initial tray-bone alignment in anterior-posterior, posterior slope, and varus-valgus degrees of freedom have a considerable impact on the interface micromotions. We suggest that some caution should be taken when using marker relative displacements between exposed surfaces to assess actual interface micromotions. The validated cadaveric models presented in this study could be used for further pre-clinical assessment of new TKR designs.

#### CRediT author statement

Huizhou Yang – Methodology, Investigation, Validation, Writing - Original Draft, Writing - Review & Editing

Riza Bayoglu – Methodology, Investigation, Validation, Writing - Original Draft, Writing - Review & Editing

Mohsen Sharifi Renani – Methodology, Investigation

Yashar Behnam – Methodology, Investigation

Alessandro Navacchia – Methodology

Chadd Clary – Conceptualization, Methodology, Supervision, Project administration, Funding acquisition

Paul J. Rullkoetter – Conceptualization, Methodology, Writing - Review & Editing, Supervision, Project administration, Funding acquisition

#### Declaration of competing interest

The authors declare that they have no known competing financial interests or personal relationships that could have appeared to influence the work reported in this paper.

#### Acknowledgements

This study was supported in part by DePuy Synthes Products, Inc (Warsaw, IN).

#### References

- Abdul-Kadir, M.R., Hansen, U., Klabunde, R., Lucas, D., Amis, A., 2008. Finite element modelling of primary hip stem stability: the effect of interference fit. *J. Biomech.* 41 (3), 587–594. <https://doi.org/10.1016/j.biomech.2007.10.009>.
- Anderson, M.J., Keyak, J.H., Skinner, H.B., 1992. Compressive mechanical properties of human cancellous bone after gamma irradiation. *J. Bone Joint Surg.* 74 (5), 747–752. <https://doi.org/10.2106/00004623-199274050-00014>.
- Bhimji, S., Meneghini, R.M., 2012. Micromotion of cementless tibial baseplates under physiological loading conditions. *J. Arthroplasty* 27 (4), 648–654. <https://doi.org/10.1016/j.arth.2011.06.010>.
- Bhimji, S., Meneghini, R.M., 2014. Micromotion of cementless tibial baseplates: keels with adjuvant pegs offer more stability than pegs alone. *J. Arthroplasty* 29 (7), 1503–1506. <https://doi.org/10.1016/j.arth.2014.02.016>.
- Bragdon, C.R., Burke, D., Lowenstein, J.D., OConnor, D.O., Ramamurti, B., Jasty, M., Harris, W.H., 1996. Differences in stiffness of the interface between a cementless porous implant and cancellous bone in vivo in dogs due to varying amounts of implant motion. *J. Arthroplasty* 11 (8), 945–951. [https://doi.org/10.1016/s0883-5403\(96\)80136-7](https://doi.org/10.1016/s0883-5403(96)80136-7).
- Camine, V.M., Rüdiger, H., Pioletti, D., Terrier, A., 2016. Full-field measurement of micromotion around a cementless femoral stem using micro-CT imaging and radiopaque markers. *J. Biomech.* 49 (16), 4002–4008. <https://doi.org/10.1016/j.jbiomech.2016.10.029>.
- Chong, D.Y., Hansen, U.N., Amis, A.A., 2010. Analysis of bone-prosthesis interface micromotion for cementless tibial prosthesis fixation and the influence of loading conditions. *J. Biomech.* 43 (6), 1074–1080. <https://doi.org/10.1016/j.jbiomech.2009.12.006>.
- Crook, P.D., Owen, J.R., Hess, S.R., Al-Humadi, S.M., Wayne, J.S., Jiranek, W.A., 2017. Initial stability of cemented vs cementless tibial components under cyclic load. *J. Arthroplasty* 32 (8), 2556–2562. <https://doi.org/10.1016/j.arth.2017.03.039>.
- Dalury, D.F., 2016. Cementless total knee arthroplasty: current concepts review. *The Bone and Joint Journal* 98 (B), 867–873. <https://doi.org/10.1302/0301-620X.98B7.37367>, 7th ser.
- Eberle, S., Göttlinger, M., Augat, P., 2013. Individual density-elasticity relationships improve accuracy of subject-specific finite element models of human femurs. *J. Biomech.* 46 (13), 2152–2157. <https://doi.org/10.1016/j.jbiomech.2013.06.035>.
- Fitzpatrick, C.K., Maag, C., Clary, C.W., Metcalfe, A., Langhorn, J., Rullkoetter, P.J., 2016. Validation of a new computational 6-DOF knee simulator during dynamic activities. *J. Biomech.* 49 (14), 3177–3184. <https://doi.org/10.1016/j.jbiomech.2016.07.040>.
- Godeset, A.C., Beaugonin, M., Haug, E., Taylor, M., Gregson, P.J., 2002. Simulation of a knee joint replacement during a gait cycle using explicit finite element analysis. *J. Biomech.* 35, 267–275. [https://doi.org/10.1016/S0021-9290\(01\)00179-8](https://doi.org/10.1016/S0021-9290(01)00179-8).
- Halloran, J.P., Petrella, A.J., Rullkoetter, P.J., 2005. Explicit finite element modeling of total knee replacement mechanics. *J. Biomech.* 38 (2), 323–331. <https://doi.org/10.1016/j.jbiomech.2004.02.046>.
- Hashemi, A., Shirazi-Adl, A., 2000. Finite element analysis of tibial implants — effect of fixation design and friction model. *Comput. Methods Biomed. Eng.* 3 (3), 183–201. <https://doi.org/10.1080/10255840008915264>.
- Kaneko, T.S., Bell, J.S., Pejcic, M.R., Tehrani-Zadeh, J., Keyak, J.H., 2004. Mechanical properties, density and quantitative CT scan data of trabecular bone with and without metastases. *J. Biomech.* 37 (4), 523–530. <https://doi.org/10.1016/j.jbiomech.2003.08.010>.
- Kraemer, W.J., Harrington, I.J., Hearn, T.C., 1995. Micromotion secondary to axial, torsional, and shear loads in two models of cementless tibial components. *J. Arthroplasty* 10 (2), 227–235. [https://doi.org/10.1016/s0883-5403\(05\)80132-9](https://doi.org/10.1016/s0883-5403(05)80132-9).
- Kurtz, S.M., Lau, E., Ong, K., Zhao, K., Kelly, M., Bozic, K.J., 2009. Future Young patient demand for primary and revision joint replacement: national projections from 2010 to 2030. *Clin. Orthop. Relat. Res.* 467 (10), 2606–2612. <https://doi.org/10.1007/s11999-009-0834-6>.
- Linde, F., Hvid, I., Madsen, F., 1991. The effect of specimen size and geometry on the mechanical behaviour of trabecular bone specimens. *J. Biomech.* 24 (6), 454. [https://doi.org/10.1016/0021-9290\(91\)90046-p](https://doi.org/10.1016/0021-9290(91)90046-p).
- Navacchia, A., Clary, C.W., Wilson, H.L., Behnam, Y.A., Rullkoetter, P.J., 2018. Validation of model-predicted tibial tray-synthetic bone relative motion in cementless total knee replacement during activities of daily living. *J. Biomech.* 77, 115–123. <https://doi.org/10.1016/j.jbiomech.2018.06.024>.
- Newman, J.M., Sodhi, N., Khlopas, A., Sultan, A.A., Chughtai, M., Abraham, R., Mont, M. A., 2018. Cementless total knee arthroplasty: a comprehensive review of the literature. *Orthopedics* 41 (5), 263–273. <https://doi.org/10.3928/01477447-20180815-05>.
- Norman, T.L., Ackerman, E.S., Smith, T.S., Gruen, T.A., Yates, A.J., Blaha, J.D., Kish, V. L., 2006. Cortical bone viscoelasticity and fixation strength of press-fit femoral stems: an in-vitro model. *J. Biomech. Eng.* 128 (1), 13. <https://doi.org/10.1115/1.2133766>.
- Pilliar, R.M., Lee, J.M., Maniatopoulos, C., 1986. Observations on the effect of movement on bone ingrowth into porous-surfaced implants. *Clinical Orthopaedics and Related Research, &NA;*(208). <https://doi.org/10.1097/00003086-198607000-00023>.
- Shultz, T.R., Blaha, J.D., Gruen, T.A., Norman, T.L., 2006. Cortical bone viscoelasticity and fixation strength of press-fit femoral stems: a finite element model. *J. Biomech. Eng.* 128 (1), 7. <https://doi.org/10.1115/1.2133765>.
- Taylor, M., Barrett, D.S., Deffenbaugh, D., 2012. Influence of loading and activity on the primary stability of cementless tibial trays. *J. Orthop. Res.* 30 (9), 1362–1368. <https://doi.org/10.1002/jor.22056>.
- Verdonschot, N., Huiskes, R., 1996. Mechanical effects of stem cement interface characteristics in total hip replacement. *Clinical Orthopaedics & Related Research*, 329 326–336. <https://doi.org/10.1097/00003086-199608000-00040>.
- Yildirim, G., Gopalakrishnan, A., Davignon, R.A., Parker, J.W., Chawla, H., Pearl, A.D., 2016. Comparative fixation and subsidence profiles of cementless unicompartmental

knee arthroplasty implants. *J. Arthroplasty* 31 (9), 2019–2024. <https://doi.org/10.1016/j.arth.2016.02.034>.

Yoshii, I., Whiteside, L.A., Milliano, M.T., White, S.E., 1992. The effect of central stem and stem length on micromovement of the tibial tray. *J. Arthroplasty* 7, 433–438. [https://doi.org/10.1016/s0883-5403\(07\)80036-2](https://doi.org/10.1016/s0883-5403(07)80036-2).

Zannoni, C., Mantovani, R., Viceconti, M., 1999. Material properties assignment to finite element models of bone structures: a new method. *Med. Eng. Phys.* 20 (10), 735–740. [https://doi.org/10.1016/s1350-4533\(98\)00081-2](https://doi.org/10.1016/s1350-4533(98)00081-2).